



Attenuation of BPA degradation by $\text{SO}_4^{\cdot-}$ in a system of peroxymonosulfate coupled with Mn/Fe MOF-templated catalysts and its synergism with Cl^- and bicarbonate



Xiaojie Qiu^a, Shengjiong Yang^{a,*}, Mawuli Dzakpasu^a, Xiaoping Li^a, Dahu Ding^b, Pengkang Jin^a, Rongzhi Chen^c, Qionghua Zhang^a, Xiaochang C. Wang^a

^a Key Laboratory of Environmental Engineering, Xi'an University of Architecture and Technology, No. 13, Yanta Road, Xi'an, Shaanxi 710055, China

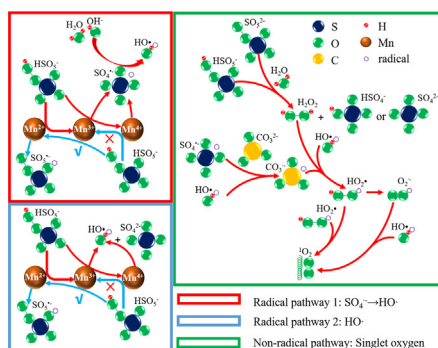
^b College of Resources and Environmental Sciences, Nanjing Agricultural University, No. 1, Weigang, Nanjing, Jiangsu 210095, China

^c College of Resources and Environment, University of Chinese Academic of Science, 19A, Yuquan Road, Beijing 100049, China

HIGHLIGHTS

- Porous $\text{Mn}_{0.8}\text{Fe}_{2.2}\text{O}_4$ MNCs was successfully developed through Mn/Fe bi-MOFs template.
- MNCs exhibited desirable adsorption capacity, rendering better degradation performance.
- $\text{HO}\cdot$ was the dominant radical for BPA degradation in MNCs/PMS system.
- Surface-bound radicals might play a crucial role in MNCs/PMS system.

GRAPHICAL ABSTRACT



ARTICLE INFO

Keywords:
 MOFs
 Peroxymonosulfate
 PMS
 Singlet oxygen
 Manganese ferrite

ABSTRACT

$\text{Mn}_{0.8}\text{Fe}_{2.2}\text{O}_4$ magnetic nanocrystals ($\text{Mn}_{0.8}\text{Fe}_{2.2}\text{O}_4$ MNCs) are synthesized by thermal treatment of a metal-organic framework (MOF) template, and their physicochemical properties are characterized in detail. The $\text{Mn}_{0.8}\text{Fe}_{2.2}\text{O}_4$ MNCs exhibited highly efficient performance for the catalytic degradation of Bisphenol A (BPA) by peroxymonosulfate (PMS) activation at various initial pH, catalyst dosage, and PMS concentration. A leaching solution experiment evidenced that PMS activation by the $\text{Mn}_{0.8}\text{Fe}_{2.2}\text{O}_4$ MNCs is a heterogeneous process. Interestingly, scavenging experiments and electron paramagnetic resonance (EPR) analysis demonstrated that $\text{HO}\cdot$ is the dominant radical for BPA degradation, rather than $\text{SO}_4^{\cdot-}$. The scavenger experiment indicated that the surface-bound radicals may play the crucial role for BPA degradation. Increasing Cl^- or decreasing bicarbonate concentrations in solution enhanced the catalytic degradation process significantly through non-radical pathways. The $\text{Mn}_{0.8}\text{Fe}_{2.2}\text{O}_4$ MNCs exhibited desirable stability and reusability, that the spent $\text{Mn}_{0.8}\text{Fe}_{2.2}\text{O}_4$ MNCs could be significantly regenerated by thermal treatment at 450°C in open air. Findings from this study would expand the applications of MOFs and also provide new insights into the enhancement of degradation efficiency during PMS activation processes.

* Corresponding author.

E-mail address: yangshengjiong@xauat.edu.cn (S. Yang).

<https://doi.org/10.1016/j.cej.2019.04.175>

Received 2 February 2019; Received in revised form 10 April 2019; Accepted 26 April 2019

Available online 26 April 2019

1385-8947/ © 2019 Elsevier B.V. All rights reserved.

1. Introduction

The radicals of hydroxyl ($\text{HO}\cdot$) and sulfate ($\text{SO}_4^{\cdot-}$) are widely employed for the degradation of bio-undegradable organic pollutants [1]. Thus, the development of advanced oxidation processes (AOPs) based on $\text{HO}\cdot$ and $\text{SO}_4^{\cdot-}$ have attracted increasing attention in the past years [2]. Initial attempts at the degradation of various organic contaminants such as pesticides [3], dyes [4], phenols [5] and antibiotics [6,7] with $\text{HO}\cdot/\text{SO}_4^{\cdot-}$ -AOPs exhibited efficient performances. It was also evidenced that $\text{SO}_4^{\cdot-}$ is more effective for the degradation of organic matter due to its higher redox potential (2.5–3.1 V) than $\text{HO}\cdot$ (1.9–2.7 V) [8,9]. $\text{SO}_4^{\cdot-}$ can be generated by activating peroxy-monosulfate (PMS: HSO_5^-) and peroxydisulfate (PDS: $\text{S}_2\text{O}_8^{2-}$) through diverse processes, including transition metals [10], heating [11], ultraviolet radiation [12], ultrasound [13], microwave [14], and photocatalysis [15]. Among these, transition metals exhibit superiority because no external energy is required, rendering more convenience in its application.

For PMS/PDS activation by transition metal activation, the spinel ferrite with the general formula of MFe_2O_4 has exhibited great potential in the degradation of organic pollutants. Therefore, diverse MFe_2O_4 ($\text{M} = \text{Co}, \text{Mn}, \text{Cu}, \text{Zn}, \text{and Ni}$) have been synthesized to improve the activation of PMS/PDS to generate $\text{SO}_4^{\cdot-}$. Among these, cobalt ferrite exhibited the highest catalytic efficiency for the degradation of organic pollutants [16,17]. However, the secondary pollution caused by the leaching of Co, as well as its high cost hindered its further application. Therefore, manganese ferrite, with a comparatively low cost and without any secondary pollution, is deemed as a promising material for the activation of PMS/PDS. A body of evidence suggests that the coupling of manganese ferrite nanoparticles with PMS/PDS could significantly degrade organic pollutants [18]. Nonetheless, as known, the efficiency of a catalytic process usually depends on the mass/electron transfer efficiency, which is correlated with the surface area and pore structure of catalysts [8,19]. However, manganese ferrite catalysts fabricated through traditional processes, such as co-precipitation and sol-gel, are incapable of obtaining catalysts with high specific surface areas and porous structures, rendering low catalytic capabilities [20]. Therefore, manganese ferrite catalysts with high specific surface area and well-defined porous structure are highly desired.

Metal-organic frameworks (MOFs), carbonaceous crystalline materials coordinated by metal cations and organic linkers, exhibit large internal surface areas and high pore volumes. MOFs are deemed as excellent precursors to fabricate various metal oxides with well-defined porous structures through suitable thermal treatment [21,22]. It is reported that porous Co_3O_4 derived from Co-MOF-74 exhibited significantly increased performance as an anode material in an ion battery [23]. Fe_3C fabricated from Fe-MOF also exhibited higher hexavalent chromium adsorption capacity [24]. Therefore, the development of similar processes for the fabrication of manganese ferrite might produce catalysts with high specific surface area and well-defined porous structure for the degradation of organic pollutants.

BPA (2,2-bis(4-hydroxyphenyl)propane) is an endocrine disrupting compound that is extensively used in the production of plastics, phenol resins and epoxy resins [25]. Due to its widespread applications, BPA has invariably been detected in drinking water and the bodies of wildlife and human beings [26]. Therefore, BPA represents a potential threat to humankind and ecosystems [27]. Burgeoning studies have trialed several methods for the removal of BPA such as adsorption [28], extraction [29], biodegradation [30], Fenton degradation [31], and photodegradation [32], among others. However, these methods usually suffer from various disadvantages, such as low efficiency, secondary pollution, complicated operation, etc. [33]. More effective processes for BPA removal are, therefore, highly desired.

Herein, [Mn/Fe(acac-bdc)] (bdc: p-Phthalic acid, acac: acetylacetonate) bimetallic MOFs (Mn/Fe bi-MOFs) were developed as a template for the synthesis of porous manganese ferrite catalysts through

suitable pyrolysis treatment. The obtained catalyst was carefully characterized and was then used to activate PMS for the catalytic degradation of BPA. The effects of various conditions including solution pH, catalysts dosage, and PMS concentration were evaluated. Also, the reusability and stability of the catalysts were assessed. Furthermore, the synergism between the system and anions is discussed in detail. The possible mechanism of PMS activation in the current system is also proposed.

2. Material and method

2.1. Chemicals

Iron(III) acetylacetonate ($(\text{Fe}(\text{acac})_3$, 98%), p-Phthalic acid ($\text{C}_8\text{H}_6\text{O}_4$, 99%), Oxone ($\text{KHSO}_5 \cdot 0.5\text{KHSO}_5 \cdot 0.5\text{K}_2\text{SO}_4$), Tert-butanol (TBA), Furfuryl alcohol (FFA), 5,5-di-methyl-1-pyrrolidine N-oxide (DMPO), and 2,2,6,6-Tetramethyl-4-piperidinol (TEMP) were purchased from Shanghai Macklin Biochemical Co., Ltd (Shanghai, China). Manganese chloride ($\text{MnCl}_2 \cdot 4\text{H}_2\text{O}$, 99%), Sodium chloride (NaCl, 99.5%), Sodium carbonate anhydrous (Na_2CO_3 , 99.8%), and sodium bicarbonate (NaHCO_3 , 99.8%) were obtained from Kermel Chemical Reagent Co., Ltd (Tianjin, China). Ethanol, dimethylformamide (DMF, 99.5%), and Bisphenol A (BPA, 99%) were obtained from Aladdin Chemical Co., Ltd (Shanghai, China). Methanol and acetonitrile were purchased from Thermo Fisher. All reagents were at least analytical grade and used without any purification. All solutions were prepared by dissolving the reagents in ultrapure water ($> 18 \text{ M}\Omega\text{-cm}$, produced by Milli-Q, German) [34].

2.2. Preparation of catalyst

The catalysts were prepared by hydrothermal method. Typically, 1 mmol $\text{Fe}(\text{acac})_3$, 1.67 mmol PTA, and 0.5 mmol $\text{MnCl}_2 \cdot 4\text{H}_2\text{O}$ were thoroughly dissolved in 15 mL ethanol and 25 mL DMF at room temperature with vigorous stirring. Then the resulting homogeneous solution was transferred into a Teflon Lined autoclave which was subsequently incubated in an electric oven at 120°C for 12 h. After natural cooling to room temperature, the products were collected by centrifugation at 12000 rpm for 10 min and washed with ethanol for three times. The solid product was dried at 60°C to obtain the Mn/Fe bi-MOFs. Mn/Fe MNCs were obtained after thermal treatment of the Mn/Fe bi-MOFs at 450°C for 1 h with a temperature ramp of $10^\circ\text{C min}^{-1}$. The Fe-MOFs ($\text{Fe}(\text{acac-bdc})$)-derived catalyst was synthesized using the same procedure but without the addition of $\text{MnCl}_2 \cdot 4\text{H}_2\text{O}$ during the reaction.

2.3. Degradation of BPA

Unless otherwise stated, the degradation experiments were carried out in 150 mL glass vessels at room temperature. Before the reaction, the solution pH was adjusted to 6.5 with HNO_3 (0.1 M) or NaOH (0.1 M) to avoid the effect of coexisting Cl^- . Typically, Mn/Fe MNCs (0.1 g L^{-1}) were evenly dispersed into 100 mL BPA solution (concentration: $40 \mu\text{M}$) by sonication. The solution was stirred for 10 min to achieve an adsorption/desorption equilibrium between BPA and the catalysts. Then, varying amounts of PMS at 0.2, 0.4, 0.8, 2 mM were added into the solution to initiate the degradation reaction. At desired time intervals, 1.0 mL reaction solution was withdrawn, filtered with a $0.22 \mu\text{m}$ filter into an HPLC vial and quenched with 0.5 mL methanol immediately. The spent catalyst was collected with a magnet after each reaction cycle, which was then dried at 60°C prior to the next cycle.

2.4. Characterization and analytical methods

The fabricated materials were characterized by field emission scanning electron microscopy (FESEM, Quanta FEG, 250), transmission

electron microscopy (TEM, FEI Tecnai G2 F20), X-ray diffraction (XRD, Rigaku Ultimate IV), vibrating sample magnetometry (VSM, Lake Shore 7307), Thermogravimetric (TG) analysis (STA 449 F3 Jupiter®), N₂ sorption/desorption analysis (V-sorb 2800P), and X-ray photoelectron spectrometry (XPS, Thermo Fisher K-Alpha). Besides, electron paramagnetic resonance (EPR, Bruker EMXmicro-6/1) was used to determine the relative intensity of reactive oxidation species in the reaction system. Total organic carbon (TOC) was measured by using a TOC analyzer (TOC-V CPH). Detailed information about the characteristics of the catalysts is shown in the [Supplementary Material](#). The BPA concentration was quantified by ultra-high-performance liquid chromatography (UHPLC, Thermofisher, Ultimate 3000, USA) equipped with a DAD detector (detection wavelength: 278 nm) and a Thermo-scientific 1.7 μm BEH C18 column (100 mm*2.1 mm). The mobile phase consisted of acetonitrile/water (v/v, 50/50) at a flow rate of 0.2 mL min⁻¹. The concentration of Fe and Mn ions was analyzed by an inductively coupled plasma mass spectrometry (ICP-MS, NexION™ 350D).

3. Results and discussion

3.1. Characterization

The morphological structures, regular spindle-like shapes, and surface element characterization of the Fe-MOFs and Mn/Fe bi-MOFs are shown in [Fig. S1](#) to [Fig. S4](#).

The thermal stability of the Fe-MOFs and Mn/Fe bi-MOFs, determined by thermogravimetric analysis ([Fig. 1a](#)), indicates the total weight loss of 74.08% (Fe-MOFs) and 72.71% (Mn/Fe bi-MOFs) within the temperature range of 20 to 600 °C in open air. Specifically, the thermogravimetric process of Mn/Fe bi-MOFs in open air can be divided into two stages, 40–310 °C and 310–475 °C, which can be

ascribed to the losses of crystalline/coordinated water or organic solution and the pyrolysis of carbonaceous structure, respectively. Similar stages of 40–340 °C and 340–448 °C can be observed during the pyrolysis of Fe-MOFs. In addition, as can be noted in [Fig. 1a](#), a weak endothermic peak occurs on the Differential Scanning Calorimeter (DSC) curve at the preliminary stage, which is attributable to the vaporization heat of the crystalline water and residual organic solution. Notably, a typical exothermic peak (426.5 °C) was found in the DSC curve during the pyrolysis of Fe-MOFs, indicating the complete formation of resulting metal oxide. However, this exothermic peak occurred at 452.8 °C during the pyrolysis of Mn/Fe bi-MOFs, which is obviously higher than that of Fe-MOFs, indicating the different phase of metal oxide after pyrolysis of Fe-MOFs and Mn/Fe bi-MOFs.

XRD patterns were recorded to evidence the crystallinities and phases of the fabricated MOFs and MNCs. As shown in [Fig. 1b](#), the phases and crystallinities of Fe-MOFs and Mn/Fe bi-MOFs are identically different. The diffraction peaks positioned at lower 2-theta degree, indicating that both MOFs have carbonaceous crystal structures in nature. The pattern also demonstrates that Mn in the MOFs acted as the central ions, and slightly affected the crystallinities and phases of the resulting MOFs, which further evidenced the FESEM observation. The diffraction peaks of the fabricated Fe-MOFs and Mn/Fe bi-MOFs exhibited in [Table S1](#) demonstrated their apparent differences.

XRD analysis further proved the conclusion of TG analysis that the thermal treatment of the Fe-MOFs and Mn/Fe bi-MOFs changed the phase and crystallinity of the obtained catalysts significantly. As shown in [Fig. 1c](#), the phase of the Fe-MOFs-derived catalyst can be identified as Fe₂O₃ (JCPDS No. 33-0664) (Fe₂O₃ MNCs), whereby diffraction peaks positioned at 24.12°, 33.15°, 35.61°, 40.85°, 49.48°, 54.09°, 62.45°, and 63.99°, respectively, corresponding to the Bragg planes of (0 1 2), (1 0 4), (1 1 0), (1 1 3), (0 2 4), (1 1 6), (2 1 4), and (3 0 0). By contrast, the Mn/Fe bi-MOFs-derived catalysts matches the standard

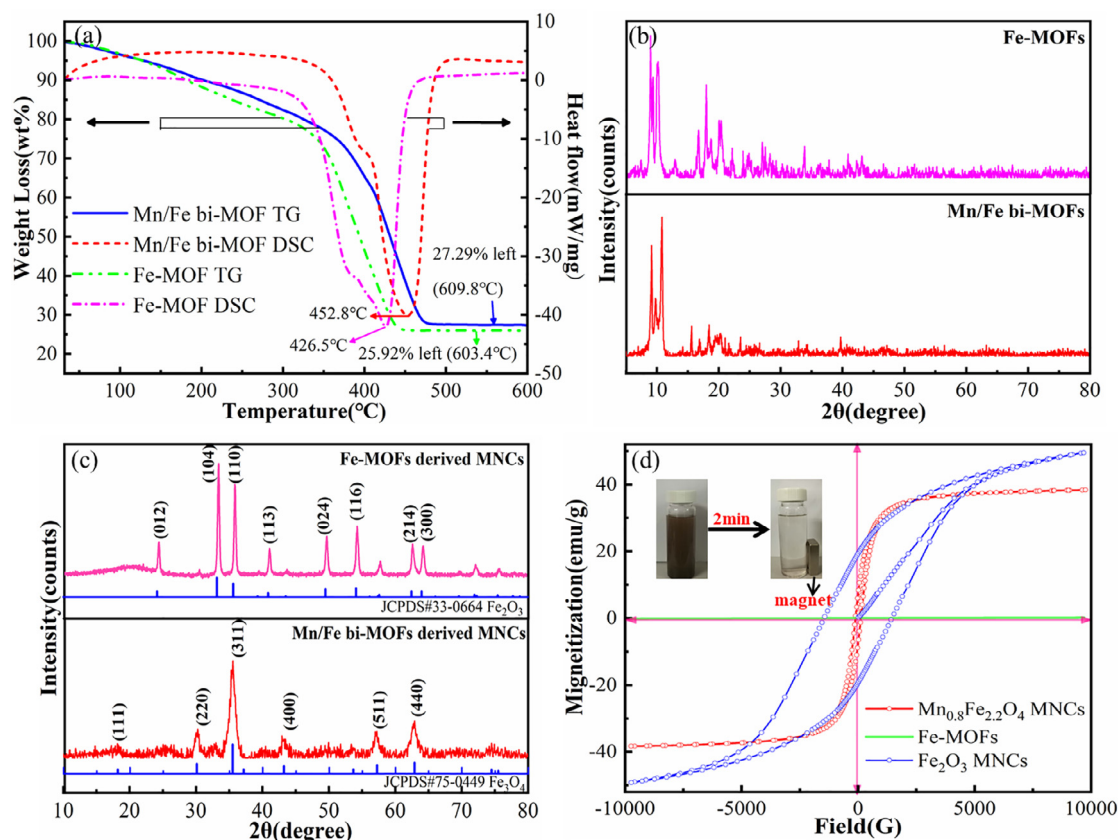


Fig. 1. (a) Thermogravimetric curves of Fe-MOFs and Mn/Fe bi-MOFs; (b) XRD patterns of Fe-MOFs and Mn/Fe bi-MOFs; (c) XRD patterns of Fe-MOFs and Mn/Fe bi-MOFs derived catalysts; (d) magnetic hysteresis loops via VSM analysis of Fe₂O₃ and Mn_{0.8}Fe_{2.2}O₄ MNCs.

Fe_3O_4 (JCPDS No. 75–0449) with identical diffraction peaks occurring at 2-theta of 18.45°, 30.36°, 35.76°, 43.47°, 57.51°, 63.16°, respectively, corresponding to the Bragg planes of (1 1 1), (2 2 0), (3 1 1), (4 0 0), (5 1 1), (4 4 0). No impurities were observed in the pattern, indicating the single phase of the obtained catalysts. It is interesting that a Mn-involved phase cannot be found by the XRD analysis of the resulting catalysts. Therefore, the catalysts were thoroughly digested by aqua regia and, afterward, analyzed with an ICP-MS to evidence its chemical composition. The results demonstrate the coexistence of both Mn and Fe with a molar ratio of 1: 2.73 (Mn: Fe, Table S2). This finding indicates that the catalyst is manganese ferrite with a similar crystal structure to Fe_3O_4 , but with some Fe being substituted by Mn. Similar results have been reported, whereby manganese ferrite exhibited the same diffraction characteristic as Fe_3O_4 [35]. Therefore, the structural formula of the catalysts obtained by Mn/Fe bi-MOFs can be defined as $\text{Mn}_{0.8}\text{Fe}_{2.2}\text{O}_4$. This structural formula was further evidenced by EDX analysis that the molar ratio of Mn: Fe on the surface of the catalysts is 1: 2.54, which is very close to the result obtained from the ICP-MS analysis (Fig. S4). Overall, the obtained results clearly evidenced that the resulting catalyst was manganese ferrite with the structural formula of $\text{Mn}_{0.8}\text{Fe}_{2.2}\text{O}_4$ ($\text{Mn}_{0.8}\text{Fe}_{2.2}\text{O}_4$ MNCs). The average crystallite size of the $\text{Mn}_{0.8}\text{Fe}_{2.2}\text{O}_4$ MNCs, calculated using the Scherrer formula (Eq. S1), indicated an average of 52 nm. In addition, it should be noted that the Mn-MOFs, which used Mn^{2+} as the cation sources in the absence of Fe^{3+} , cannot be synthesized in the same way, indicating that Mn^{2+} cannot be employed as the only central ions in an acac-bdc ligand system.

The resulting catalysts were further characterized by VSM analysis to evaluate their ferromagnetism. As shown in Fig. 1d, Fe_2O_3 MNCs exhibited obvious ferromagnetic behavior with the saturation magnetization (M_s) of 49.5 emu/g, indicating that the catalyst is ferrite. Nevertheless, the M_s decreased to 38.26 emu/g for $\text{Mn}_{0.8}\text{Fe}_{2.2}\text{O}_4$ MNCs, possibly due to the replacement of magnetic Fe with the diamagnetic Mn. Nonetheless, the dispersed $\text{Mn}_{0.8}\text{Fe}_{2.2}\text{O}_4$ MNCs could be separated from water with a magnet in 2 min, rendering the convenience in separating the catalysts from solution. The magnetic parameters of Fe_2O_3 and $\text{Mn}_{0.8}\text{Fe}_{2.2}\text{O}_4$ MNCs were shown in Table S3.

The FESEM and TEM analyses further verified the morphological structure of $\text{Mn}_{0.8}\text{Fe}_{2.2}\text{O}_4$ MNCs. Whereas the FESEM image of $\text{Mn}_{0.8}\text{Fe}_{2.2}\text{O}_4$ MNCs (Fig. 2a) demonstrated its uniform rod-like microstructure, the TEM images (Fig. 2b and c) further revealed that it consisted of various microparticles. Moreover, the Fast Fourier Transformation (FFT) pattern (Fig. 2e) derived from the HRTEM image (Fig. 2d) confirmed the crystallinity of the $\text{Mn}_{0.8}\text{Fe}_{2.2}\text{O}_4$ MNCs with bright rings corresponding to the (1 1 1), (3 1 1), (4 0 0), and (5 1 1) planes, which agree with the XRD results. Furthermore, the lattice spaces, identified from a line scan analysis of the HRTEM image (Fig. 2g) indicate crystal lattice fringes with d-spacing of 0.250 nm that can be assigned to the (3 1 1) planes of the spinel system (marked in Fig. 2d and 2f). The line scans analysis of (1 1 1) and (4 0 0) are shown in Fig. S5. The EDX mapping on the surface of $\text{Mn}_{0.8}\text{Fe}_{2.2}\text{O}_4$ MNCs (Fig. 2i–k) showed that Fe, Mn, and O were distributed uniformly in the $\text{Mn}_{0.8}\text{Fe}_{2.2}\text{O}_4$ MNCs, indicating the formation of Mn/Fe bimetallic oxides. This observation provides further evidence that the resulting catalysts are manganese ferrite. The FESEM image and element mapping of Fe_2O_3 MNCs were shown in Fig. S6, that a longer particle size than $\text{Mn}_{0.8}\text{Fe}_{2.2}\text{O}_4$ MNCs could be observed with the same shape.

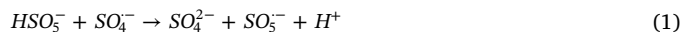
The N_2 adsorption/desorption isotherms and pore size distribution of $\text{Mn}_{0.8}\text{Fe}_{2.2}\text{O}_4$ MNCs shown in Fig. S7 corresponds to a type-III isotherm, according to the adsorption materials classification of IUPAC, indicating its well-defined mesoporous structure [36]. The pore size distribution shows the coexistence of mesopores and macropores. The desirable BET surface area and pore volume of the $\text{Mn}_{0.8}\text{Fe}_{2.2}\text{O}_4$ MNCs of $50.75 \text{ m}^2 \text{ g}^{-1}$ and $0.13 \text{ cm}^3 \text{ g}^{-1}$ indicated a strong interaction between catalysts and solution, therefore, rendering higher mass-transfer efficiency. Thus, highly efficient catalytic performance can be expected.

The properties of the prepared $\text{Mn}_{0.8}\text{Fe}_{2.2}\text{O}_4$ MNCs are summarized in Table S2.

3.2. Catalytic performance

The catalytic degradation of BPA was carried out at an initial pH (pH_0) of 6.5 to exclude the base activation of PMS [37]. Fig. 3 shows the BPA degradation under various reaction conditions. It should be noted that $\text{Mn}_{0.8}\text{Fe}_{2.2}\text{O}_4$ MNCs could adsorb about 26% of BPA and achieve an adsorption equilibrium within 10 min of reaction, possibly due to its well-defined porous structure. Therefore, in the current study, the catalysts were firstly put in contact with the BPA solutions for 10 min before PMS was added to activate the catalytic degradation process. It also should be noted that PMS alone cannot effectively degrade BPA, and can account for less than 2% of BPA removal.

The effect of PMS concentration shown in Fig. 3a demonstrates that increasing PMS concentrations from 0.04 to 0.4 mM significantly enhance the catalytic performance slightly. The reaction constant k obtained with the pseudo-first-order kinetic model increased with the PMS concentrations from 0.021 min^{-1} to 0.068 min^{-1} (Fig. S8). This increase in k could be explained by the generation of more free radicals with increasing PMS concentrations when coupled with the catalysts [38]. However, the reaction rate sharply decreases to 0.039 min^{-1} when the PMS concentration is further increased to 2 mM, indicating that certain inhibitory effects occurred when excessive PMS coexisted in solution. This phenomenon has been widely reported, whereby excessive PMS could quench $\text{SO}_4^{\cdot-}$ and HO^{\cdot} [39] (Eqs. (1) and (2)). Hence, a PMS concentration of 0.4 mM was determined as suitable for the catalytic degradation processes. In addition, the Fe_2O_3 MNCs was unable to adequately activate PMS, so that less than 5% of BPA was degraded after the adsorption stage. This finding further evidenced the significance of Mn in the catalysts.



The effect of catalyst dosage illustrated in Fig. 3b demonstrates a remarkable enhancement to BPA degradation with increasing $\text{Mn}_{0.8}\text{Fe}_{2.2}\text{O}_4$ MNCs dosage. This finding can be explained by the significant increase in the functional active sites for better PMS activation with increasing catalyst dosages in the reaction system [40,41]. Moreover, the BPA degradation was completed quickly within 20 min when the catalyst dosage increased to 0.5 g L^{-1} . A correlation analysis between k and catalysts dosage (inset in Fig. 3b) shows a linear correlation of $k = 0.4574[\text{catalyst dosage}] + 0.0062$ with a coefficient of $R^2 = 0.9893$. This finding provides additional evidence to highlight the enhancement of BPA degradation with increasing catalysts dosages.

The effects of pH_0 were further evaluated by varying pH_0 at 4.0, 6.5, and 10.2. The results presented in Fig. 3c indicates a strong effect of pH_0 on the BPA adsorption efficiency, whereby the adsorption efficiency of BPA decreased with increasing pH_0 of 4.0, 6.5 and 10.2 at 41.6%, 33.8%, and 28.8%, respectively. A pK_a of 9.6 has been reported for BPA, which would speciate into anionic form (BPA^{2-}) within the pH range of 6–12 (Fig. S9) [42]. In addition, the point of zero charge (pH_{pzc}) of manganese ferrite was determined to be 7.4 through potentiometric titration. Therefore, at $\text{pH}_0 > \text{pH}_{\text{pzc}}$, the surface of $\text{Mn}_{0.8}\text{Fe}_{2.2}\text{O}_4$ MNCs was negatively charged, and so BPA^{2-} could hardly be adsorbed to the surface of $\text{Mn}_{0.8}\text{Fe}_{2.2}\text{O}_4$ MNCs due to the electrostatic repulsion. On the contrary, at $\text{pH}_0 < \text{pH}_{\text{pzc}}$, the surface of $\text{Mn}_{0.8}\text{Fe}_{2.2}\text{O}_4$ MNCs would be positively charged so that both BPA^0 and BPA^{2-} could be easily adsorbed by the $\text{Mn}_{0.8}\text{Fe}_{2.2}\text{O}_4$ MNCs. Therefore, the BPA adsorption efficiency was largely increased at lower initial pH_0 . However, Fig. 3c demonstrates an opposite result in the catalytic stage compared with the adsorption stage, whereby the catalytic performance is significantly higher at pH_0 of 10.2 than that at 4.0 and 6.0. Furthermore, the reaction rate showed considerable increases of 0.036,

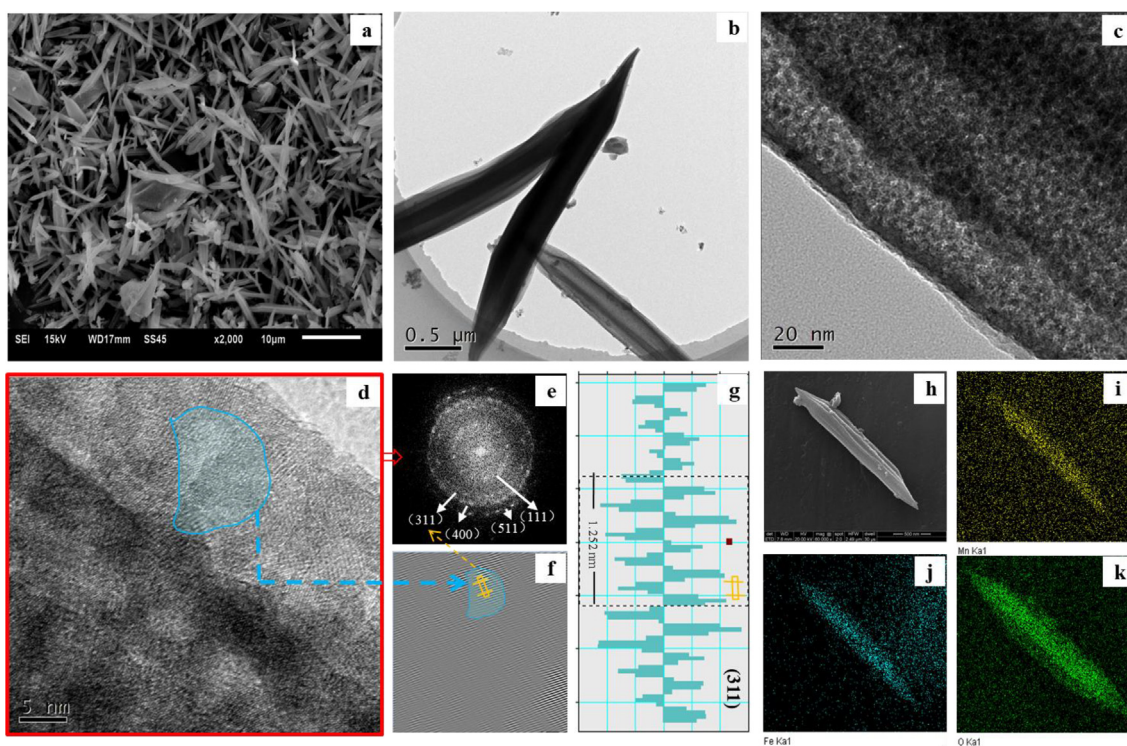
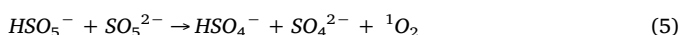


Fig. 2. Characterization of Mn/Fe bi-MOFs derived $\text{Mn}_{0.8}\text{Fe}_{2.2}\text{O}_4$ MNCs: (a) FESEM image; (b-c) TEM images; (d) HRTEM image; (e) FFT pattern derived from image (d); (f) inverse FFT pattern of (3 1 1) plane; (g) line scan of HRTEM image in the yellow area of (f), indicating a lattice fringe spacing of 0.250 nm, corresponding to (3 1 1) Bragg plane; (h-k) EDX element mapping of Mn, Fe and O obtained from (h).

0.048, and 0.062 with increasing pH_0 of 4.0, 6.5, and 10.2, respectively. These increase might be mainly attributed to the scavenging effects of H^+ on $\text{SO}_4^{\cdot-}$ and $\text{HO}\cdot$, which can be described by Eqs. (3) and (4) [43]. It should be noted that the solution pH would be strongly affected by PMS addition. In the current system, the variation of solution pH after PMS addition at different pH_0 is illustrated in Fig. S10. The solution pH immediately decreased to 3.9, 4.9, and 9.4 at the pH_0 of 4.0, 6.5, and 10.2, respectively. Further gradual decreases in the solution pH were noted with time until equilibrium was attained at 3.6, 3.8, and 5.3, respectively. Therefore, it can be explained that the activity of H^+ is high under acidic conditions, rendering a reinforced scavenging effect. On the contrary, the activity of H^+ largely decreased under basic conditions to weaken the scavenging effect. Besides, increased pH could enhance the decomposition rate of PMS, rendering the formation of singlet oxygen, consequently, increasing the catalytic performance (Fig. S11, Eq. (5)) [44]. Generally, the catalytic performance is better at a slightly alkaline pH_0 .



The stability of $\text{Mn}_{0.8}\text{Fe}_{2.2}\text{O}_4$ MNCs was evaluated by stirring 0.01 g of catalyst 100 mL deionized water for 60 min to obtain a leaching solution. The concentrations of Mn and Fe ions were then measured using an ICP-MS. The results demonstrated the leached Mn and Fe mass of 45.9 μg and 41.2 μg , respectively. The leaching solution was subsequently used for PMS activation. As shown in Fig. 3b, the leaching solution degraded less than 9% of BPA. Therefore, the PMS activation by $\text{Mn}_{0.8}\text{Fe}_{2.2}\text{O}_4$ MNCs is a heterogeneous process. In addition, the spent catalysts were collected by means of a magnet, and dried at 65 $^\circ\text{C}$ prior to the next runs to evaluate its reusability. As shown in Fig. 3d, the catalytic performance gradually decreased with each consecutive run,

possibly because the adsorbed organic intermediates inhibited the mass-transfer between the catalysts and PMS. It should be noted that the spent catalyst could be largely recovered by thermal treatment in open air at 450 $^\circ\text{C}$ for 15 min. The recovery can be ascribed to the pyrolysis of adsorbed intermediates during the thermal treatment process, thus, rendering a re-exposed surface of catalysts for the next run. The XRD analysis showed that the phase of the $\text{Mn}_{0.8}\text{Fe}_{2.2}\text{O}_4$ MNCs is stable after regeneration (Fig. S12). Overall, this finding demonstrates desirable reusability.

3.3. Proposed activation mechanism

Samples of the raw and spent $\text{Mn}_{0.8}\text{Fe}_{2.2}\text{O}_4$ MNCs were characterized by XPS analysis to elucidate the catalytic process further. The XPS survey spectrum shown in Fig. S13a demonstrates the existence of Mn, Fe, and O on the surface of the $\text{Mn}_{0.8}\text{Fe}_{2.2}\text{O}_4$ MNCs. The high-resolution XPS spectrum of Mn 2p shows that the Mn 2p_{3/2} can be deconvoluted as three peaks located at 641.4 eV, 642.5 eV, and 644.4 eV, respectively (Fig. 4a), which can be ascribed to the Mn (II), Mn (III) and Mn (IV) states. Before catalytic reaction, the relative contents of Mn (II), Mn (III) and Mn (IV) in the catalysts are 26.19%, 51.61%, and 22.20%, respectively. After the reaction, the relative content of Mn (II), Mn (III), and Mn (IV) changed to 39.81%, 35.83%, and 24.36%, indicating obvious valence changes of Mn during the catalytic process. As shown in Fig. 4b, the Fe 2p spectrum of the raw $\text{Mn}_{0.8}\text{Fe}_{2.2}\text{O}_4$ MNCs shows three states at the binding energies of 710.5 eV, 711.5 eV, and 713.0 eV that can be ascribed to the Oct Fe (II), Oct Fe (III), and Tet Fe (III), respectively. After catalytic reaction, the relative contents of Oct Fe (II) increased from 18.7% to 24.1%, whereas that of Tet Fe (III) decreased from 55.1% to 49.7%, indicating that Fe (II) in the catalyst partially transformed to Fe (III).

The high-resolution O 1s spectra before and after the catalytic reaction are deconvoluted into two peaks (Fig. S13b). The deconvolution of the O 1s spectra shows two peaks at 530.3 and 531.6 eV, which can

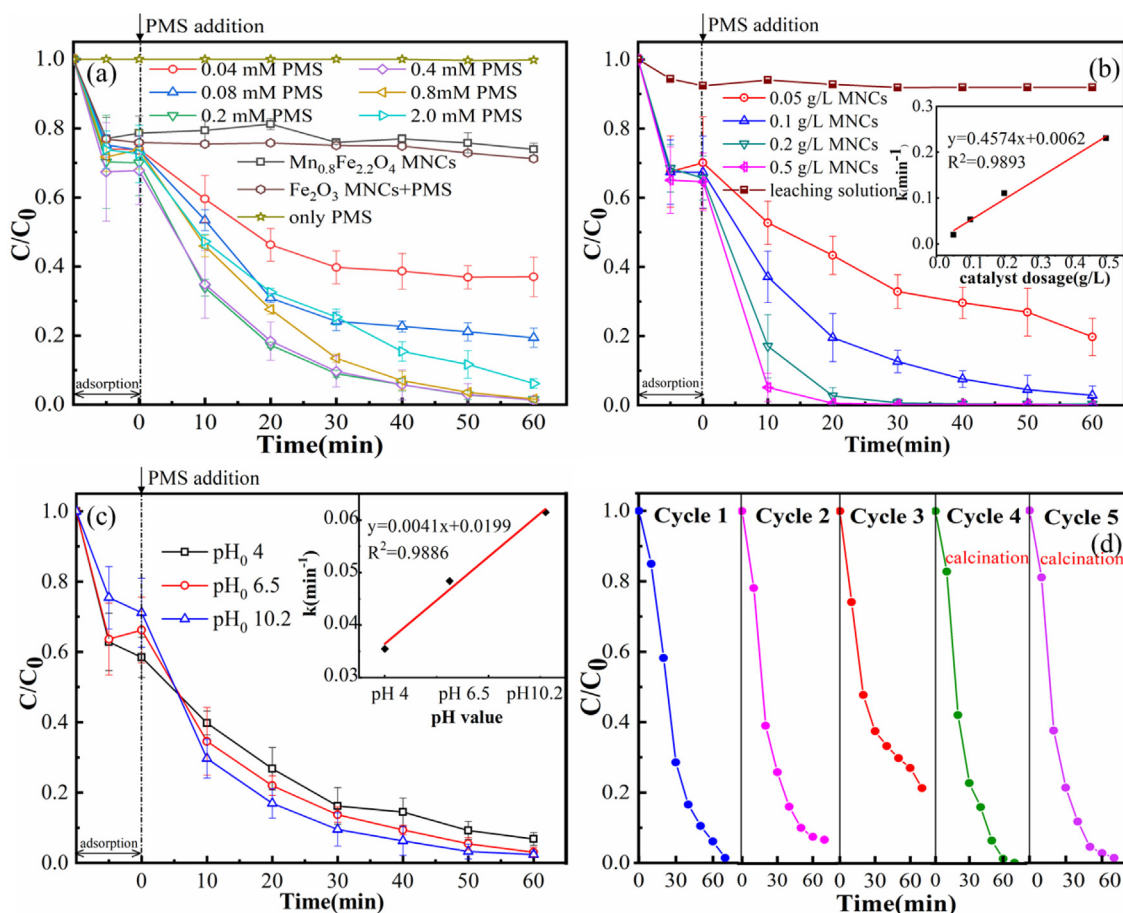


Fig. 3. Factorial effects for the catalytic degradation of BPA by $\text{Mn}_{0.8}\text{Fe}_{2.2}\text{O}_4$ MNCs: (a) effect of oxidant dosage; (b) effect of catalysts dosage; (c) effect of initial solution pH; (d) removal efficiency of BPA in multiple use of $\text{Mn}_{0.8}\text{Fe}_{2.2}\text{O}_4$ MNCs. Experimental conditions: [BPA] = 40 μM , [PMS] = 0.40 mM (0.04, 0.08, 0.2, 0.4, 0.8, 2.0 mM in Fig. 3a), [$\text{Mn}_{0.8}\text{Fe}_{2.2}\text{O}_4$ MNCs] = 0.1 g L^{-1} (0.05, 0.1, 0.2, and 0.5 g L^{-1} in Fig. 3b), [Temperature] = 25 $^{\circ}\text{C}$, [pH₀] = 6.5 (4.0, 6.5, and 10.2 in Fig. 3c).

be ascribed to the lattice oxygen (O_{β}) and adsorbed oxygen and surface hydroxyl species (O_{α}) [45]. It has been confirmed that both of those components are significantly active oxygen species for radical generation and oxidation processes [46]. After the catalytic reaction, it was found that the relative intensity of O_{β} reduced from 71.89% to 66.24%, and that of O_{α} increased from 28.11% to 33.76%. This finding indicates that O_{β} participated in the reaction process. The decrease of O_{β} in $\text{Mn}_{0.8}\text{Fe}_{2.2}\text{O}_4$ MNCs may be due to the reduction of the trivalent metal ion to a divalent metal ion (Eqs. S2 and S3) [47]. Conversely, the increase of O_{α} may be attributed to the formation of M-OH groups (M = Mn, Fe) on the surface of $\text{Mn}_{0.8}\text{Fe}_{2.2}\text{O}_4$ MNCs during the catalytic

It is well known that $\text{HO}\cdot$ and $\text{SO}_4\cdot^-$ are involved in the catalytic activation process of PMS by transition metal [48]. To identify the major reactive oxygen species (ROS) generated in the catalytic process, radical scavenging experiments were further conducted in the presence of a quencher in the catalytic system including methanol (MeOH) and tert-butyl alcohol (TBA). MeOH can be used to quench both $\text{HO}\cdot$ and $\text{SO}_4\cdot^-$ radicals, whereas TBA usually serves as an $\text{HO}\cdot$ quencher but not $\text{SO}_4\cdot^-$ [49]. As shown in Fig. 4c, when TBA (30 mM) existed in the PMS/MNCs/BPA system, the degradation efficiency of BPA sharply decreased to 48.76%, indicating the hydroxyl radical was involved in ROS. More interestingly, when MeOH (30 mM) presented in the same system, the BPA degradation rate decreased to 47.2%, which is similar to that by TBA. Furthermore, when TBA (5 mM) existed in the system, the BPA degradation rate decreased to 56.07%. When MeOH (5 mM) existed in the system, the BPA degradation rate decreased to 57.43%. This observation demonstrated that only a little $\text{SO}_4\cdot^-$ was consumed for BPA degradation in the system. Furthermore, an unusual result was

obtained if the concentration of the quencher was further increased to 200 mM and 1000 mM. As shown in Fig. 4c, TBA (200 mM) and MeOH (200 mM) exhibited negligible quenching effects and even slightly enhanced the BPA degradation when the concentration of TBA and MeOH increased to 1000 mM. This observation has been reported by only a few researchers [35]. Therefore, the shielding/masking effect caused by high concentrations of TBA and MeOH on the surface of catalysts should be noted [50]. This effect implies that at high concentrations, MeOH and TBA are hardly adsorbed on the surface of catalysts due to their physicochemical properties, such as high viscosity or hydrophilicity. Thus, although the free radicals could be easily quenched under the shielding/masking effect, the surface-bound radicals, nonetheless, could hardly be quenched under the same condition (Fig. S14). Overall, it can be summarized from the currently existing research that the shielding/masking effect usually occurred when Mn/Cu based catalysts were used for PMS/PS activation (Table S4).

EPR experiments were performed to detect the changes in the generated radical species involved in the MNCs/PMS system at different times by using DMPO as the spin-trapping agent. The results shown in Fig. 4d demonstrate the pattern of DMPO- $\cdot\text{OH}$ adducts, which provide additional evidence to support the results of the scavenging experiment that $\text{HO}\cdot$ is an involved radical. In addition, DMPO- $\text{SO}_4\cdot^-$ could be observed but at an extraordinary low intensity even within 2 min. This observation agreed well with the findings of radical quenching experiment. However, this result conflicts with the findings of most existing studies that $\text{SO}_4\cdot^-$ is the major radical species [6,51–53].



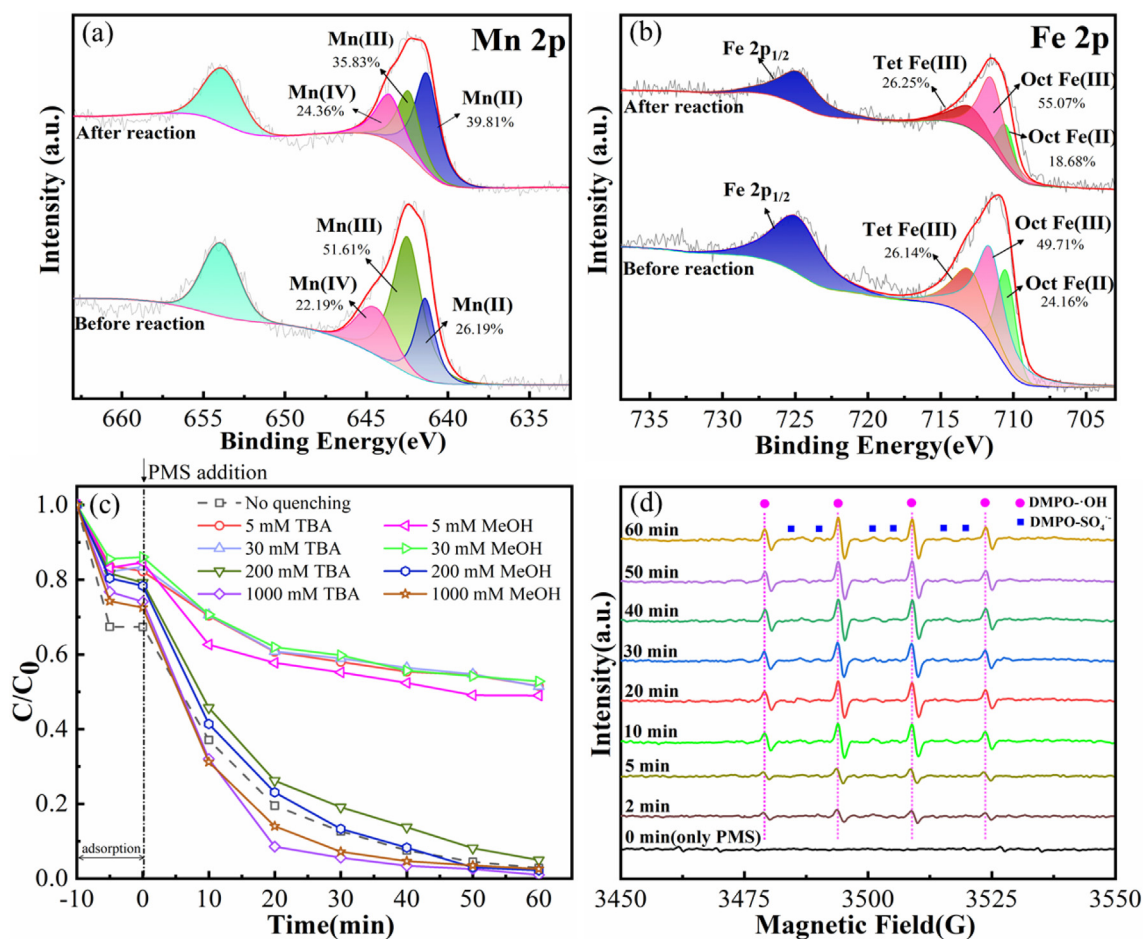
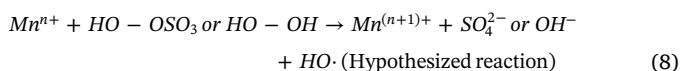


Fig. 4. (a) Mn 2p XPS spectra of the fresh and spent $\text{Mn}_{0.8}\text{Fe}_{2.2}\text{O}_4$ MNCs; (b) Fe 2p XPS spectra of the fresh and spent $\text{Mn}_{0.8}\text{Fe}_{2.2}\text{O}_4$ MNCs; (c) Effect of different radical quenchers on BPA degradation in $\text{Mn}_{0.8}\text{Fe}_{2.2}\text{O}_4$ MNCs/PMS system. Experimental conditions: [BPA] = 40 μM , [PMS] = 0.4 mM, [$\text{Mn}_{0.8}\text{Fe}_{2.2}\text{O}_4$ MNCs] = 0.1 g L⁻¹, [Temperature] = 25 °C, [pH₀] = 6.5; (d) EPR spectra obtained by using DMPO as spin-trapping agent in $\text{Mn}_{0.8}\text{Fe}_{2.2}\text{O}_4$ MNCs/PMS system.



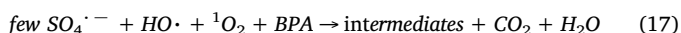
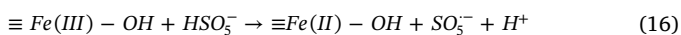
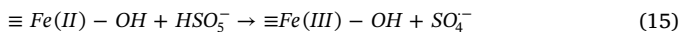
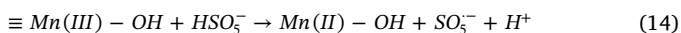
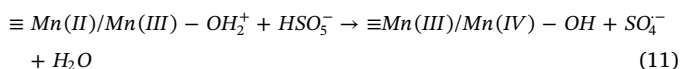
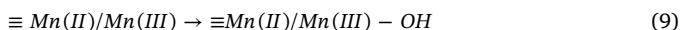
As known, the generation of $\text{HO}\cdot$ in the PMS activation process can be described by Eqs. (6) and (7). Therefore, considering the ineffective generation of $\text{SO}_4^{\cdot-}$ in current system, extra pathways might exist with respect to the significantly generated $\text{HO}\cdot$. Hence, we attempted to identify any other possible pathways through which $\text{HO}\cdot$ may be generated in the current system. The activation of PMS by transition metals is a Fenton-like reaction. Nonetheless, PMS (HO-OSO_3) is a substituted derivative of H_2O_2 (HO-OH) in which one H atom is replaced with an SO_3^- group [54]. Considering the similarity between H_2O_2 and PMS, we hypothesize that $\text{HO}\cdot$ can be directly generated through the process described by Eq. (8) like $\text{Fe}^{2+}/\text{H}_2\text{O}_2$ system. Therefore, the MNCs/ H_2O_2 reaction system was employed to determine whether $\text{HO}\cdot$ can be generated through a Fenton process by $\text{Mn}^{2+/3+}$. The reaction was conducted at pH₀ of 10.2 to weaken the adsorption efficiency. As shown in Fig. S15, less than 4% of BPA was degraded after adsorption stage by MNCs/ H_2O_2 system (H_2O_2 : 4 mM). Moreover, about 13% of BPA was degraded when the concentration of H_2O_2 was increased to 100 mM. This result implies that H_2O_2 could be activated by $\text{Mn}_{0.8}\text{Fe}_{2.2}\text{O}_4$ MNCs to directly generate $\text{HO}\cdot$. The high-resolution XPS spectrum of Mn 2p of the spent catalysts obtained after H_2O_2 activation (Fig. S16) shows that the relative contents of Mn (II), Mn (III) and Mn (IV) changed from 26.19%, 51.61%, and 22.19% to 16.67%, 46.67%, and 36.67% after the reaction, respectively. Thus, Mn (II)/(III) was obviously consumed,

whereas the content of Mn (IV) notably increased, indicating an electron losing process of Mn (II) \rightarrow III \rightarrow IV) during the H_2O_2 activation process. Therefore, the hypothesized reaction (Eq. (8)) likely occurred. In addition, the metal species occurred in various valence states in the current system, including Fe (II)/(III) and Mn (II)/(III)/(IV). The occurrence of these metal species with diverse valence states causes the formation of large surface hydroxyl groups by their hydrolysis (Fig. S13), which, consequently may increase the reaction rate with $\text{SO}_4^{\cdot-}$ into $\text{HO}\cdot$, possibly rendering the difficulty in $\text{SO}_4^{\cdot-}$ detection by EPR analysis. Therefore, it can be concluded that the $\text{HO}\cdot$ is generated in the current system by (1) $\text{Mn}^{\text{II/III}}$ activated Fenton reaction and (2) the reaction between $\text{SO}_4^{\cdot-}$ and $\text{H}_2\text{O}/\text{OH}^-$.

In addition, it must be noted that the valence change of Mn after PMS activation is largely different to that after H_2O_2 activation (Fig. S16). While the relative content of Mn (III) decreased from 51.61% to 35.83%, that of Mn (II) increased from 26.19% to 39.18% after the PMS activation, respectively. This result demonstrates that Mn could be reduced during the PMS activation process, which is significantly different to that of the H_2O_2 activation process whereby Mn (II) and Mn (III) in the $\text{Mn}_{0.8}\text{Fe}_{2.2}\text{O}_4$ MNCs could only be oxidized to Mn (III) and Mn (IV), but Mn (IV) and Mn (III) could not be reduced to Mn (III) and Mn (II). In the current MNCs/PMS system, the redox potentials of existing pairs are 1.71 V (Mn (III)/Mn (II)), 2.5–3.1 V ($\text{HSO}_5^-/\text{SO}_4^{\cdot-}$), and 1.1 V ($\text{HSO}_5^-/\text{SO}_5^{\cdot-}$). Therefore, the redox potential of Mn (III)/Mn (II) falls between $\text{HSO}_5^-/\text{SO}_5^{\cdot-}$ and $\text{HSO}_5^-/\text{SO}_4^{\cdot-}$, thus, rendering the redox cycle of Mn (II) \rightarrow III \rightarrow II) thermodynamically favorable. Moreover, the Mn valence change after PMS activation also

demonstrates that Mn (IV) cannot be reduced into Mn (III), possibly due to its very low redox potential (0.975 V), rendering its stable chemical property [46].

Therefore, the following possible mechanism could be proposed: $\equiv\text{Mn}$ (II) and $\equiv\text{Mn}$ (III) on the surface of the catalysts combine with hydroxyl groups through dissociative adsorption of water molecules to form $\equiv\text{Mn}$ (II)/(III)–OH (Eq. (9)). Under an acidic condition, manganese hydroxyl is protonated and transformed into $\equiv\text{Mn}$ (II)/(III)–OH₂⁺ due to the higher pH_{zpc} of the catalysts (Eq. (10)). The generated $\equiv\text{Mn}$ (II)/(III)–OH₂⁺ species on the surface of the catalyst adsorb PMS electrostatically to produce additional surface-bound SO₄·[−] (Eq. (11)). HO· is produced by the SO₄·[−] and Mn (II → III → IV) process afterward (Eqs. (8) and (12)–(13)). Moreover, SO₅·[−] are produced during the redox cycle of Mn (II → III → II) (Eq. (14)). Furthermore, the $\equiv\text{Fe}$ (II)–OH₂⁺ species formed on the surface of the MNCs could react with PMS to generate SO₄·[−] and HO· (Eq. (15)). However, the redox cycle of Fe (II → III → II) is thermodynamically unfavorable because it recorded the lowest redox potential (0.77 V) in the current system (Eq. (16)) [55]. In addition, other metal valence states, including Mn (IV) and Fe (III), could supply more protonated surface hydroxyl sites to enhance the adsorption of PMS and BPA onto the catalyst surface. Besides, the decomposition of PMS would slightly generate ¹O₂ (Eq. (5)). Finally, the pollutant was degraded by HO·, few SO₄·[−] and ¹O₂ into intermediates or CO₂ and H₂O.



3.4. Synergism of anions on catalytic activity

Anions are widely present in natural water bodies. Therefore, the interactive effects of coexisting anions should be considered. Existing studies reported that common anions including NO₃[−], PO₄^{3−}, CO₃^{2−}/HCO₃[−], and Cl[−] exhibit different impacts on the PMS activation process [56–58]. Thus, the efficacy of the MNCs/PMS system was evaluated in the presence of different anions. Findings demonstrate that the effects of NO₃[−] and PO₄^{3−} on the catalytic process are negligible. By contrast, bicarbonate and Cl[−] exhibited significant impacts. The effect of different Cl[−] concentrations on the MNCs/PMS system was shown in Fig. S17. The BPA degradation efficiency is shown to decrease with increasing Cl[−] concentration from 1 mM to 10 mM, but further increases in the Cl[−] concentration from 20 mM to 50 mM, nonetheless, tended to enhance the degradation efficiency considerably. Reports from previous studies confirm that PMS and SO₄·[−] can oxidize Cl[−] into reactive chlorine species, such as HOCl/OCl[−] or ·Cl [58]. The reaction involved can be described according to Eqs. (18)–(25). Under low Cl[−] concentrations, the decreased BPA degradation efficiency may be caused by an inhibition effect, whereby SO₄·[−] is quenched by Cl[−] to generate lower reactive ·Cl (2.4 V), rendering the decreased catalytic performance. Conversely, under high Cl[−] concentrations, the widely generated ·Cl is finally transformed into free available reactive chlorine

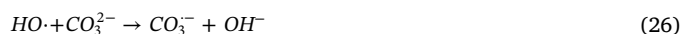
species such as HOCl/OCl[−], Cl₂, and HCl, rendering an enhanced degradation efficiency. A similar phenomenon has been reported that higher concentrations of chloride can remarkably enhance the degradation efficiency of dyes in a cobalt/PMS system [18]. In addition, EPR analysis showed that the signal intensity of ¹O₂ in the Cl[−]/MNCs/PMS system was slightly higher than that in the PMS solution, possibly indicating that PMS could be slightly activated by Cl[−] to generate ¹O₂ (Fig. S18).



Bicarbonate is ubiquitous in natural water bodies, according to Henry's law, because of atmospheric CO₂. Therefore, the influence of bicarbonate on the PMS oxidation system cannot be avoided. Thus, the effect of bicarbonate on the BPA degradation efficiency was evaluated through catalytic experiments performed at different bicarbonate concentrations (0.5–10 mM).

Fig. 5a demonstrates that low concentrations of bicarbonate significantly accelerated the catalytic degradation process. However, a high concentration of bicarbonate showed notable inhibition of the catalytic degradation process. Complete degradation of BPA could be attained in the MNCs/PMS system at the bicarbonate concentration of 1.0 mM in the solution. The reaction rate at the bicarbonate concentrations of 0.5, 1.0, 2.0, 5.0, 10.0 mM were 0.047, 0.076, 0.047, 0.024 and 0.016, respectively. Furthermore, a controlled trial conducted with PMS/bicarbonate without any dosage of the catalyst indicated that BPA could be significantly degraded (Fig. S19a). This result demonstrates that PMS can be activated by bicarbonate, whereby 0.5 mM bicarbonate could slightly activate PMS to achieve a 12.3% degradation of BPA. Moreover, when the concentration of bicarbonate was increased to 1.0 mM, significant activation of PMS could be observed, and 26.1% of BPA was degraded within 60 min. However, further increases in the bicarbonate concentration exhibited severe inhibition effects on BPA degradation, which corroborates the results obtained from the MNCs/PMS/bicarbonate system.

It could be explained that the bicarbonate significantly increases the solution pH (Fig. S19b), rendering the dissociation of HSO₅[−] into SO₅[−] to generate ¹O₂ (Eq. (5)) in the PMS/bicarbonate system. However, severe inhibition of BPA degradation occurred when the concentration of bicarbonate exceeded 2 mM in the MNCs/PMS system. Bicarbonates are usually considered as radical scavengers in oxidation reaction processes [59]. Therefore, the severe inhibition of BPA degradation under high concentrations of bicarbonate can be attributed to its quenching effect. Excessive bicarbonate would compete with BPA to react with SO₄·[−] and HO· to generate CO₃·[−]/HCO₃·[−] with much lower redox potential (E⁰ = 1.78 V) than SO₄·[−] and HO· (Eqs. 26–29). Moreover, the rate constants of CO₃·[−]/HCO₃·[−] in a reaction with organic compounds are 2–3 times lower than that of SO₄·[−] and HO· [60,61]. Therefore, bicarbonate could suppress the degradation performance of the radical degradation pathway. A similar phenomenon of the bicarbonate effect was also reported in a previous study [44].



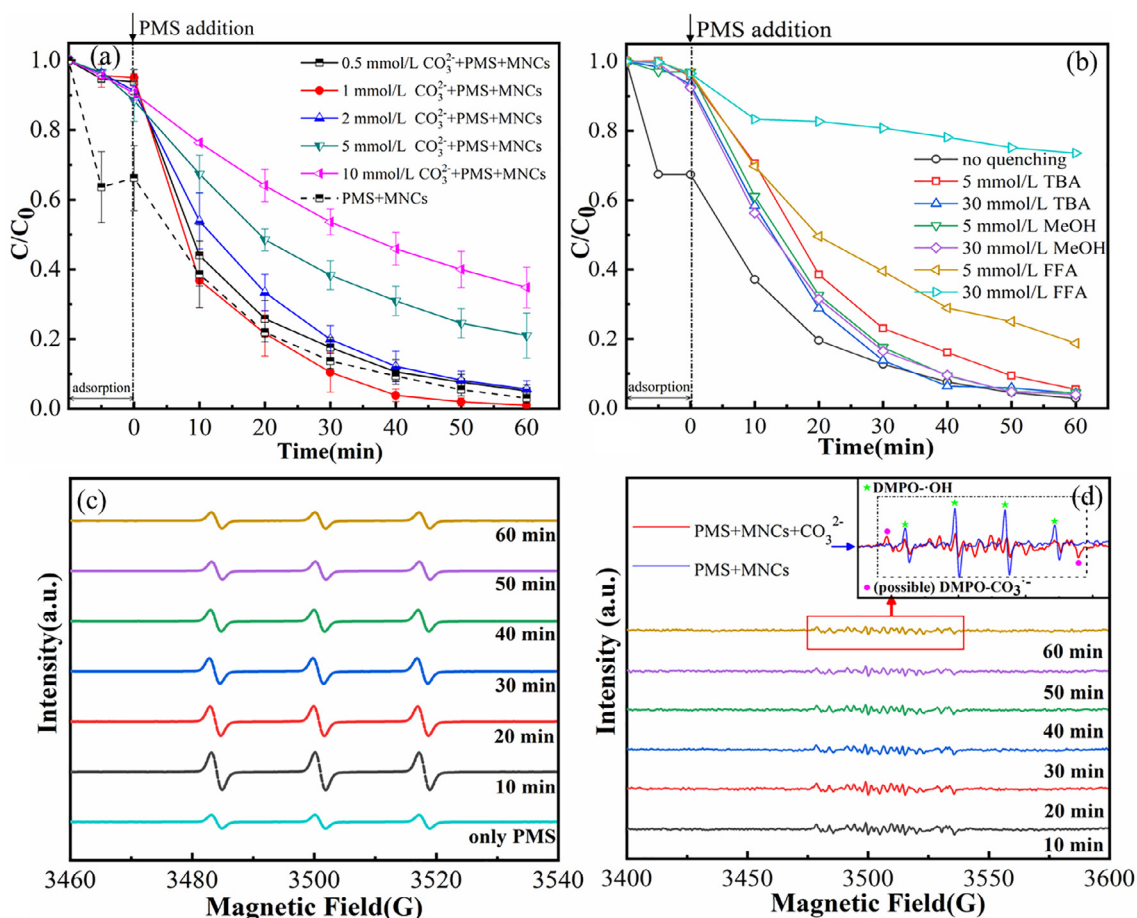


Fig. 5. (a) Effect of bicarbonate on the degradation of BPA in the Mn_{0.8}Fe_{2.2}O₄ MNCs/PMS system; (b) Effect of different radicals quenchers on BPA degradation in the Mn_{0.8}Fe_{2.2}O₄ MNCs/PMS/bicarbonate system; (c) intensity of ¹O₂ as a function of time, and EPR spectra obtained by using TEMP as a spin-trapping agent in the Mn_{0.8}Fe_{2.2}O₄ MNCs/PMS/bicarbonate system ([Na₂CO₃] = 1 mM); (d) EPR spectra obtained from the Mn_{0.8}Fe_{2.2}O₄ MNCs/PMS/bicarbonate system in the presence of DMPO ([Na₂CO₃] = 1 mM). Experimental conditions: [BPA] = 40 μM, [PMS] = 0.4 mM, [Mn_{0.8}Fe_{2.2}O₄ MNCs] = 0.1 g L⁻¹, [Temperature] = 25 °C, [pH₀] = 6.5.



The synergism of bicarbonate in the current process was elucidated through quenching experiments using TBA and MeOH at comparatively low concentrations (5 mM and 30 mM) to avoid the shielding/masking effects. Fig. 5b shows that with the presence of bicarbonate in the solution, BPA degradation exhibited similar quenching effects to that of MeOH and TBA, indicating that HO· is the dominant radical. However, the quenching efficiency was notably lower than that without bicarbonate in the solution, possibly because of the generation of ¹O₂ when bicarbonate coexisted in the solution. Therefore, furfuryl alcohol (FFA), a more potent quenching agent, was used to evaluate the system in which bicarbonate coexisted. The results show significant decreases in the BPA degradation with FFA as the quencher.

Furthermore, EPR analysis was employed to confirm the reactive oxygen species in the reaction process by using DMPO and TEMP as spin-trapping agents. Fig. S20 shows the triplet signals (¹O₂) obtained by TEMP in the PMS/bicarbonate system. The results show that the intensity of ¹O₂ in the PMS/bicarbonate system is higher than that of only PMS, which corroborates the results in Figs. S19a. Also 5c shows that the signals of ¹O₂ are highly identical in the MNCs/PMS/bicarbonate system when TEMP was used as the spin-trapping agent. The intensity of ¹O₂ in the MNCs/PMS/bicarbonate system is largely higher than that in the PMS/bicarbonate system, demonstrating that the MNCs/PMS/bicarbonate system is more effective in generating ¹O₂ than the PMS/bicarbonate system. Also, the intensity of ¹O₂ gradually

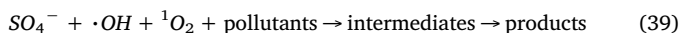
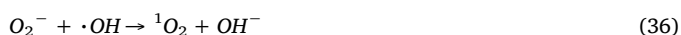
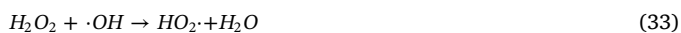
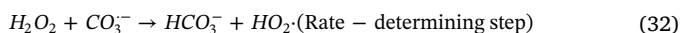
decreased with the reaction time, indicating that ¹O₂ was consumed during the BPA degradation process. This finding demonstrated the synergism between bicarbonate and the MNCs/PMS system. Results from the TOC analysis is shown in Fig. S21. About 48% of TOC was removed by the MNCs/PMS/bicarbonate system, which is notably higher than the 34% achieved by MNCs/PMS, further proving the significant synergistic effect of bicarbonate.

Furthermore, SO₄^{·-} and HO· in the MNCs/PMS/bicarbonate system were evaluated by EPR with DMPO. The results shown in Fig. 5d demonstrates that the intensities of DMPO-·OH and DMPO-SO₄^{·-} adducts in the MNCs/PMS/bicarbonate system were largely weaker than those in the MNCs/PMS system when 1 mM bicarbonate coexisted in solution. This finding suggests that substantial concentrations of HO· and SO₄^{·-} were quenched by bicarbonate. More interestingly, the EPR analysis shows a set of symmetric signals at the magnetic fields of 3478–3534 G, which has not been reported as yet. In this case, we tend to speculate that the unknown EPR spectrum in Fig. 5d might be some radical intermediates (possibly DMPO-CO₃^{·-}, inset in Fig. 5d). In general, it can be confirmed that ¹O₂ is the major species when bicarbonate is present in solution with PMS.

It is reported that PMS could decompose to generate H₂O₂ and further form HO₂[·] (Eqs. 30–32). Subsequently, HO₂[·] could generate ¹O₂ (Eq. (35)) [44]. However, the reaction rate of this process (Eq. (32)) is so slow that it inhibits the formation of HO₂[·]. In the MNCs/PMS/bicarbonate system, bicarbonate quenched HO· and SO₄^{·-} to then generate CO₃^{·-} (Eqs. 26–29). Subsequently, the CO₃^{·-} and residual HO· could react with H₂O₂ to produce moderate HO₂[·] (Eqs. (32) and

(33)). Hence, the formation of H_2O_2 was accelerated to facilitate the formation of $\text{HO}_2\cdot$ further. Thus, the generated $\text{CO}_3\cdot^-$ plays a crucial role in accelerating the formation of $\text{HO}_2\cdot$, which further promoted the formation of $^1\text{O}_2$. In addition, the generated $\text{HO}_2\cdot$ could cause the formation of $\text{O}_2\cdot^-$, and further generate H_2O_2 and $^1\text{O}_2$ as well (Eqs. 34–37). Therefore, $^1\text{O}_2$ is generated through several pathways to enhance the BPA degradation significantly. Furthermore, lower concentrations of bicarbonate (1 mM) coexisting in solution could act as a buffer that further adjusts the solution pH. The pK_a of $\text{HO}_2\cdot$ of 4.8 (Eq. (34)) indicated that more $\text{O}_2\cdot^-$ could be produced at pH higher than 4.8 to accelerate the generation of $^1\text{O}_2$ in the MNCs/PMS/bicarbonate system. The experiment also evidenced that the pH solution was changed to 10.5 when 1 mM bicarbonate existed in solution pH_0 of 6.5 (Fig. S19b), indicating that $\text{O}_2\cdot^-$ could be effectively generated. Conversely, elevated bicarbonate concentrations would quench $\cdot\text{OH}$ and $\text{SO}_4\cdot^-$ to generate $\text{CO}_3\cdot^-$, rendering a decreased BPA degradation efficiency. Previous reports also indicate that excessive bicarbonate could quench $\text{O}_2\cdot^-$ and generate OH_2^- and CO_3^{2-} (Eq. (38)) [62], further inhibiting the formation of $^1\text{O}_2$. Additionally, excessive bicarbonate may suppress the reaction between $\text{CO}_3\cdot^-$ and H_2O_2 , which could further inhibit the formation of $\text{HO}_2\cdot$ (Eq. (32)).

Overall, the suitable concentration of bicarbonate coexisting in solution could improve the catalytic performance significantly and induce an extra non-radical reactive oxidation species-dominated pathway in the MNCs/PMS/bicarbonate system. Thus, $\text{HO}\cdot$ and $^1\text{O}_2$ could effectively degrade BPA.



4. Conclusion

Ferromagnetic $\text{Mn}_{0.8}\text{Fe}_{2.2}\text{O}_4$ MNCs was synthesized for the degradation of BPA by coupling with PMS through a heterogeneous catalytic process. $\text{Mn}_{0.8}\text{Fe}_{2.2}\text{O}_4$ MNCs exhibited excellent magnetic behavior for separation, as well as stability and reusability in the degradation of the organic pollutants. Nonetheless, the results exhibited a severe attenuation of BPA degradation by $\text{SO}_4\cdot^-$, and $\cdot\text{OH}$ was the major radical to drive the BPA degradation. In addition, the results also indicated that the surface-bound radicals may play the crucial role for BPA degradation. The performance of the MNCs/PMS system was enhanced with increasing Cl^- concentrations and most notably with decreasing concentrations of bicarbonate. Moreover, $^1\text{O}_2$ could be effectively generated when 1 mM bicarbonate coexisted with PMS simultaneously. Furthermore, $\text{Mn}_{0.8}\text{Fe}_{2.2}\text{O}_4$ MNCs in a PMS/bicarbonate system could enhance the generation of $^1\text{O}_2$ by facilitating the formation of $\text{HO}_2\cdot$ and $\text{O}_2\cdot^-$. Findings from this work demonstrate that PMS activation by transition metals should be coupled with suitable concentrations of Cl^- and bicarbonate to achieve highly efficient degradation.

Acknowledgements

This research was supported by the National Natural Science Foundation of China (Grant No. 51508451) and the Natural Science Foundation of Shaanxi Province of China (Grant No. 2018JQ5140).

Appendix A. Supplementary data

Supplementary data to this article can be found online at <https://doi.org/10.1016/j.cej.2019.04.175>.

References

- [1] Q. Yang, H. Choi, S.R. Al-Abed, D.D. Dionysiou, Iron-cobalt mixed oxide nanocatalysts: heterogeneous peroxymonosulfate activation, cobalt leaching, and ferromagnetic properties for environmental applications, *Appl. Catal., B* 88 (2009) 462–469.
- [2] L. Chen, X. Zuo, S. Yang, T. Cai, D. Ding, Rational design and synthesis of hollow $\text{Co}_3\text{O}_4/\text{Fe}_2\text{O}_3$ core-shell nanostructure for the catalytic degradation of norfloxacin by coupling with peroxymonosulfate, *Chem. Eng. J.* 359 (2019) 373–384.
- [3] X.H. Sanaullah Khan, Javed Ali Khan, Hasan M. Khan, Dominic L. Boccelli, Dionysios D. Dionysiou, Kinetics and mechanism of sulfate radical- and hydroxyl radical-induced degradation of highly chlorinated pesticide lindane in UV/peroxymonosulfate system, *Chem. Eng. J.* (2017) 135–142.
- [4] L. Duan, X. Zhou, S. Liu, P. Shi, W. Yao, 3D-hierarchically structured Co_3O_4 /graphene hydrogel for catalytic oxidation of Orange II solutions by activation of peroxymonosulfate, *J. Taiwan Inst. Chem. Eng.* 76 (2017) 101–108.
- [5] G. Zhou, L. Zhou, H. Sun, H.M. Ang, M.O. Tade, S. Wang, Carbon microspheres supported cobalt catalysts for phenol oxidation with peroxymonosulfate, *Chem. Eng. Res. Des.* 101 (2015) 15–21.
- [6] L.J. Xu, W. Chu, L. Gan, Environmental application of graphene-based CoFe_2O_4 as an activator of peroxymonosulfate for the degradation of a plasticizer, *Chem. Eng. J.* 263 (2015) 435–443.
- [7] J. Yao, X. Zeng, Z. Wang, Enhanced degradation performance of sulfisoxazole using peroxymonosulfate activated by copper-cobalt oxides in aqueous solution: kinetic study and products identification, *Chem. Eng. J.* 330 (2017) 345–354.
- [8] F. Ghanbari, M. Moradi, Application of peroxymonosulfate and its activation methods for degradation of environmental organic pollutants: review, *Chem. Eng. J.* 310 (2017) 41–62.
- [9] J. Wang, S. Wang, Activation of persulfate (PS) and peroxymonosulfate (PMS) and application for the degradation of emerging contaminants, *Chem. Eng. J.* 334 (2018) 1502–1517.
- [10] G. Nie, J. Huang, Y. Hu, Y. Ding, X. Han, H. Tang, Heterogeneous catalytic activation of peroxymonosulfate for efficient degradation of organic pollutants by magnetic $\text{CuO}/\text{Fe}_3\text{O}_4$ submicron composites, *Chin. J. Catal.* 38 (2017) 227–239.
- [11] S. Yang, P. Wang, X. Yang, L. Shan, W. Zhang, X. Shao, R. Niu, Degradation efficiencies of azo dye Acid Orange 7 by the interaction of heat, UV and anions with common oxidants: persulfate, peroxymonosulfate and hydrogen peroxide, *J. Hazard. Mater.* 179 (2010) 552–558.
- [12] A. Eslami, M. Hashemi, F. Ghanbari, Degradation of 4-chlorophenol using catalyzed peroxymonosulfate with nano- MnO_2 /UV irradiation: toxicity assessment and evaluation for industrial wastewater treatment, *J. Cleaner Prod.* 195 (2018) 1389–1397.
- [13] C. Cai, L. Wang, H. Gao, L. Hou, H. Zhang, Ultrasound enhanced heterogeneous activation of peroxydisulfate by bimetallic Fe-Co/GAC catalyst for the degradation of Acid Orange 7 in water, *J. Environ. Sci.* 26 (2014) 1267–1273.
- [14] Y. Pang, H. Lei, Degradation of p-nitrophenol through microwave-assisted heterogeneous activation of peroxymonosulfate by manganese ferrite, *Chem. Eng. J.* 287 (2016) 585–592.
- [15] J. Zhang, X. Zhao, Y. Wang, Y. Gong, D. Cao, M. Qiao, Peroxymonosulfate-enhanced visible light photocatalytic degradation of bisphenol A by perylene imide-modified g-C $_3\text{N}_4$, *Appl. Catal., B* 237 (2018) 976–985.
- [16] J. Deng, S. Feng, K. Zhang, J. Li, H. Wang, T. Zhang, X. Ma, Heterogeneous activation of peroxymonosulfate using ordered mesoporous Co_3O_4 for the degradation of chloramphenicol at neutral pH, *Chem. Eng. J.* 308 (2017) 505–515.
- [17] R. Zhou, J. Zhao, N. Shen, T. Ma, Y. Su, H. Ren, Efficient degradation of 2,4-dichlorophenol in aqueous solution by peroxymonosulfate activated with magnetic spinel FeCo_2O_4 nanoparticles, *Chemosphere* 197 (2018) 670–679.
- [18] Y. Yao, Y. Cai, F. Lu, F. Wei, X. Wang, S. Wang, Magnetic recoverable $\text{MnFe}_2(\text{O})_4$ and $\text{MnFe}_2(\text{O})_4$ -graphene hybrid as heterogeneous catalysts of peroxymonosulfate activation for efficient degradation of aqueous organic pollutants, *J. Hazard. Mater.* 270 (2014) 61–70.
- [19] B. Jiang, Y. Yao, R. Xie, D. Dai, W. Lu, W. Chen, L. Zhang, Enhanced generation of reactive oxygen species for efficient pollutant elimination catalyzed by hemin based on persistent free radicals, *Appl. Catal., B* 183 (2016) 291–297.
- [20] R.T. Olsson, G. Salazar-Alvarez, M.S. Hedenqvist, U.W. Gedde, F. Lindberg, S.J. Savage, Controlled synthesis of near-stoichiometric cobalt ferrite nanoparticles, *Chem. Mater.* 17 (2005) 5109–5118.
- [21] C. Liang, X. Zhang, F. Ping, H. Chai, Y. Huang, ZIF-67 derived hollow cobalt sulfide as superior adsorbent for effective adsorption removal of ciprofloxacin antibiotics, *Chem. Eng. J.* 344 (2018) 95–104.
- [22] S. Li, X. Zhang, Y. Huang, Zeolitic imidazolate framework-8 derived nanoporous

- carbon as an effective and recyclable adsorbent for removal of ciprofloxacin antibiotics from water, *J. Hazard. Mater.* 321 (2017) 711–719.
- [23] J. Chen, X. Mu, M. Du, Y. Lou, Porous rod-shaped Co₃O₄ derived from Co-MOF-74 as high-performance anode materials for lithium ion batteries, *Inorg. Chem. Commun.* 84 (2017) 241–245.
- [24] G. Gao, L. Nie, S. Yang, P. Jin, R. Chen, D. Ding, X.C. Wang, W. Wang, K. Wu, Q. Zhang, Well-defined strategy for development of adsorbent using metal organic frameworks (MOF) template for high performance removal of hexavalent chromium, *Appl. Surf. Sci.* 457 (2018) 1208–1217.
- [25] M. Noszczyńska, Z. Piotrowska-Seget, Bisphenols: application, occurrence, safety, and biodegradation mediated by bacterial communities in wastewater treatment plants and rivers, *Chemosphere* 201 (2018) 214–223.
- [26] T. Geens, L. Goeyens, A. Covaci, Are potential sources for human exposure to bisphenol-A overlooked? *Int. J. Hyg. Environ. Health* 214 (2011) 339–347.
- [27] H.B. Pionke, D.W. Glotfelty, Contamination of groundwater by atrazine and selected metabolites, *Chemosphere* 21 (1990) 813–822.
- [28] G. Liu, J. Ma, X. Li, Q. Qin, Adsorption of bisphenol A from aqueous solution onto activated carbons with different modification treatments, *J. Hazard. Mater.* 164 (2009) 1275–1280.
- [29] Y. Geng, M. Ding, H. Chen, H.-F. Li, J.-M. Lin, Preparation of hydrophilic carbon-functionalized magnetic microspheres coated with chitosan and application in solid-phase extraction of bisphenol A in aqueous samples, *Talanta* 89 (2012) 189–194.
- [30] A. Cydzik-Kwiatkowska, K. Bernat, M. Zielińska, K. Bułkowska, I. Wojnowska-Baryła, Aerobic granular sludge for bisphenol A (BPA) removal from wastewater, *Int. Biodeterior. Biodegrad.* 122 (2017) 1–11.
- [31] W. Chen, C. Zou, Y. Liu, X. Li, The experimental investigation of bisphenol A degradation by Fenton process with different types of cyclodextrins, *J. Ind. Eng. Chem.* 56 (2017) 428–434.
- [32] L. Xu, L. Yang, E.M.J. Johansson, Y. Wang, P. Jin, Photocatalytic activity and mechanism of bisphenol A removal over TiO₂-x/rGO nanocomposite driven by visible light, *Chem. Eng. J.* 350 (2018) 1043–1055.
- [33] T. Olmez-Hanci, I. Arslan-Alaton, B. Genc, Bisphenol A treatment by the hot persulfate process: oxidation products and acute toxicity, *J. Hazard. Mater.* 263 (2013) 283–290.
- [34] S. Yang, X. Qiu, P. Jin, M. Dzakpasu, X.C. Wang, Q. Zhang, L. Zhang, L. Yang, D. Ding, W. Wang, K. Wu, MOF-templated synthesis of CoFe₂O₄ nanocrystals and its coupling with peroxymonosulfate for degradation of bisphenol A, *Chem. Eng. J.* 353 (2018) 329–339.
- [35] G.-X. Huang, C.-Y. Wang, C.-W. Yang, P.-C. Guo, H.-Q. Yu, Degradation of bisphenol A by peroxymonosulfate catalytically activated with Mn_{1.8}Fe_{1.2}O₄ nanospheres: synergism between Mn and Fe, *Environ. Sci. Technol.* 51 (2017) 12611–12618.
- [36] X. Wang, W. Wen, J. Mi, X. Li, R. Wang, The ordered mesoporous transition metal oxides for selective catalytic reduction of NO_x at low temperature, *Appl. Catal., B* 176–177 (2015) 454–463.
- [37] C. Qi, X. Liu, J. Ma, C. Lin, X. Li, H. Zhang, Activation of peroxymonosulfate by base: implications for the degradation of organic pollutants, *Chemosphere* 151 (2016) 280–288.
- [38] P. Shukla, H. Sun, S. Wang, H.M. Ang, M.O. Tadé, Co-SBA-15 for heterogeneous oxidation of phenol with sulfate radical for wastewater treatment, *Catal. Today* 175 (2011) 380–385.
- [39] M. Xu, J. Li, Y. Yan, X. Zhao, J. Yan, Y. Zhang, B. Lai, X. Chen, L. Song, Catalytic degradation of sulfamethoxazole through peroxymonosulfate activated with expanded graphite loaded CoFe₂O₄ particles, *Chem. Eng. J.* 369 (2019) 403–413.
- [40] F. Qi, W. Chu, B. Xu, Ozonation of phenacetin in associated with a magnetic catalyst CuFe₂O₄: the reaction and transformation, *Chem. Eng. J.* 262 (2015) 552–562.
- [41] G. Gan, P. Zhao, X. Zhang, J. Liu, J. Liu, C. Zhang, X. Hou, Degradation of Pantoprazole in aqueous solution using magnetic nanoscaled Fe₃O₄/CeO₂ composite: effect of system parameters and degradation pathway, *J. Alloys Compd.* 725 (2017) 472–483.
- [42] T.M. Berhane, J. Levy, M.P.S. Krekeler, N.D. Danielson, Adsorption of bisphenol A and ciprofloxacin by palygorskite-montmorillonite: effect of granule size, solution chemistry and temperature, *Appl. Clay Sci.* 132–133 (2016) 518–527.
- [43] Y.H. Huang, Y.F. Huang, C.I. Huang, C.Y. Chen, Efficient decolorization of azo dye Reactive Black B involving aromatic fragment degradation in buffered Co²⁺/PMS oxidative processes with a ppb level dosage of Co²⁺-catalyst, *J. Hazard. Mater.* 170 (2009) 1110–1118.
- [44] Y. Wang, D. Cao, X. Zhao, Heterogeneous degradation of refractory pollutants by peroxymonosulfate activated by CoOx-doped ordered mesoporous carbon, *Chem. Eng. J.* 328 (2017) 1112–1121.
- [45] R. Li, J. Kong, H. Liu, P. Chen, G. Liu, F. Li, W. Lv, A sulfate radical based ferrous-peroxydisulfate oxidative system for indomethacin degradation in aqueous solutions, *RSC Adv.* 7 (2017) 22802–22809.
- [46] Y. Yao, Y. Cai, G. Wu, F. Wei, X. Li, H. Chen, S. Wang, Sulfate radicals induced from peroxymonosulfate by cobalt manganese oxides (CoMn_{3-x}O₄) for Fenton-Like reaction in water, *J. Hazard. Mater.* 296 (2015) 128–137.
- [47] R. Polnišar, M. Štolcová, M. Hronec, M. Mikula, Structure and reactivity of copper iron pyrophosphate catalysts for selective oxidation of methane to formaldehyde and methanol, *Appl. Catal., A* 400 (2011) 122–130.
- [48] C. Wang, J. Kang, P. Liang, H. Zhang, H. Sun, M.O. Tadé, S. Wang, Ferric carbide nanocrystals encapsulated in nitrogen-doped carbon nanotubes as an outstanding environmental catalyst, *Environ. Sci. Nano* 4 (2017) 170–179.
- [49] F. Gong, L. Wang, D. Li, F. Zhou, Y. Yao, W. Lu, S. Huang, W. Chen, An effective heterogeneous iron-based catalyst to activate peroxymonosulfate for organic contaminants removal, *Chem. Eng. J.* 267 (2015) 102–110.
- [50] J. Du, J. Bao, Y. Liu, S.H. Kim, D.D. Dionysiou, Facile preparation of porous Mn/Fe₃O₄ cubes as peroxymonosulfate activating catalyst for effective bisphenol A degradation, *Chem. Eng. J.* (2018), <https://doi.org/10.1016/j.cej.2018.05.177>.
- [51] Y. Zhao, X. Ma, P. Xu, H. Wang, Y. Liu, A. He, Elemental mercury removal from flue gas by CoFe₂O₄ catalyzed peroxymonosulfate, *J. Hazard. Mater.* 341 (2018) 228–237.
- [52] Y. Xu, J. Ai, H. Zhang, The mechanism of degradation of bisphenol A using the magnetically separable CuFe₂O₄/peroxymonosulfate heterogeneous oxidation process, *J. Hazard. Mater.* 309 (2016) 87–96.
- [53] C. Tan, N. Gao, Y. Deng, J. Deng, S. Zhou, J. Li, X. Xin, Radical induced degradation of acetaminophen with Fe₃O₄ magnetic nanoparticles as heterogeneous activator of peroxymonosulfate, *J. Hazard. Mater.* 276 (2014) 452–460.
- [54] M. Nie, W. Zhang, C. Yan, W. Xu, L. Wu, Y. Ye, Y. Hu, W. Dong, Enhanced removal of organic contaminants in water by the combination of peroxymonosulfate and carbonate, *Sci. Total Environ.* 647 (2019) 734–743.
- [55] Q. Yang, X. Yang, Y. Yan, C. Sun, H. He, D. Wang, Heterogeneous activation of peroxymonosulfate by different ferromanganese oxides for tetracycline degradation: structure dependence and catalytic mechanism, *Chem. Eng. J.* 348 (2018) 263–270.
- [56] Y. Zhang, Q. Zhang, J. Hong, Sulfate radical degradation of acetaminophen by novel iron-copper bimetallic oxidation catalyzed by persulfate: mechanism and degradation pathways, *Appl. Surf. Sci.* 422 (2017) 443–451.
- [57] S. Jorfi, B. Kakavandi, H.R. Motlagh, M. Ahmadi, N. Jaafarzadeh, A novel combination of oxidative degradation for benzotriazole removal using TiO₂ loaded on FeII/FeIII/O₄C as an efficient activator of peroxymonosulfate, *Appl. Catal., B* 219 (2017) 216–230.
- [58] Y. Liu, H. Guo, Y. Zhang, W. Tang, X. Cheng, H. Liu, Activation of peroxymonosulfate by BiVO₄ under visible light for degradation of Rhodamine B, *Chem. Phys. Lett.* 653 (2016) 101–107.
- [59] L. Zhou, W. Song, Z. Chen, G. Yin, Degradation of organic pollutants in wastewater by bicarbonate-activated hydrogen peroxide with a supported cobalt catalyst, *Environ. Sci. Technol.* 47 (2013) 3833–3839.
- [60] J. Sharma, I.M. Mishra, D.D. Dionysiou, V. Kumar, Oxidative removal of Bisphenol A by UV-C/peroxymonosulfate (PMS): kinetics, influence of co-existing chemicals and degradation pathway, *Chem. Eng. J.* 276 (2015) 193–204.
- [61] Y. Ji, C. Dong, D. Kong, J. Lu, New insights into atrazine degradation by cobalt catalyzed peroxymonosulfate oxidation: kinetics, reaction products and transformation mechanisms, *J. Hazard. Mater.* 285 (2015) 491–500.
- [62] V. Můčka, V. Čuba, M. Pospíšil, R. Silber, Radiation dechlorination of some chlorinated hydrocarbons particularly of carbon tetrachloride in presence of HCO₃⁻ or NO₃⁻ ions, *Appl. Catal., A* 271 (2004) 195–201.